Biochemistry **2008,** *47,* 2265−2276

2D NMR Study of the DNA Duplex d(CTCTC*A*ACTTCC)·d(GGAAGTTGAGAG) Cross-Linked by the Antitumor-Active Dirhodium(II,II) Unit at the Cytosine−Adenine Step[†]

Mijeong Kang, Helen T. Chifotides, and Kim R. Dunbar*

Department of Chemistry, Texas A&M University, College Station, Texas 77843

Received September 17, 2007; Revised Manuscript Received October 30, 2007

ABSTRACT: The 2D NMR analysis in solution of the DNA duplex d(CTCTC*A*ACTTCC)·d(GGAAGTTGAGAG) binding to the dirhodium unit *cis*-$[Rh_2(\mu\text{-}O_2CCH_3)_2(\eta^1\text{-}O_2CCH_3)]^+$ showed that an unprecedented *intrastrand* adduct, dsII, is formed with the dirhodium unit cross-linking in the major groove residues C5 and A6 (indicated with asterisks), also corroborated by enzyme digestion studies. Formation of the dirhodium complex dsII destabilizes significantly the duplex as indicated by the substantial decrease in its melting temperature ($\Delta T_m = -22.9$ °C). The reduced thermal stability of dsII is attributed to the decreased stacking of the bases and the complete disruption and/or weakening of the hydrogen bonds within the base pairs in the immediate vicinity of the metalation site (C5·G20 and A6·T19), but the effects due to the metal binding are more severe for the base pairs in the 5′ direction to the lesion site. The NMR spectroscopic data indicate that Watson−Crick hydrogen bonding is completely disrupted for the C5·G20 site and considerably weakened for A6·T19. In dsII, the bases C5 and A6 bind to *eq* positions of the dirhodium unit *cis*-$[Rh_2(\mu\text{-}O_2CCH_3)_2(\eta^1\text{-}O_2CCH_3)]^+$, which retains one monodentate and two bridging acetate groups, presumably due to steric reasons. Binding of A6 takes place via N7, whereas binding of the C5 base takes place via the exocyclic N4 site, resulting in the *anti*-cytosine rotamer with respect to site N3 in its metal-stabilized rare iminooxo form.

In spite of the phenomenal success of cisplatin and related platinum compounds as anticancer drugs (*1*−*3*), a need has risen for new types of antitumor agents due to the limitations of platinum drugs, i.e., natural and acquired resistance of tumor cells, in addition to the numerous deleterious side effects (*4*−*7*). In this vein, dirhodium(II) tetracarboxylate derivatives (*8*) emerged as one of the most promising classes of antitumor-active transition-metal compounds, with $Rh_2(O_2CCH_3)_4$ being the first member in the series. Dirhodium tetraacetate exhibits a "paddlewheel" structure with four equatorial (*eq*) acetate groups bridging the dirhodium unit in a symmetrical fashion and two axial (*ax*) sites available to donor ligands (Chart 1) (*8*).

Chart 1: Structure of Dirhodium Tetraacetate

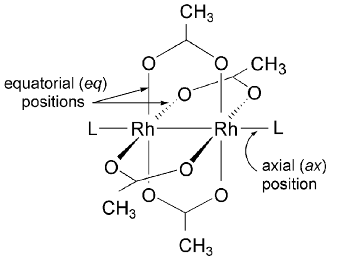

Pioneering studies that emanated in the 1970s showed that dirhodium carboxylate compounds $Rh_2(O_2CR)_4$ (R = Me, Et, Pr) exhibit significant in vivo antitumor activity against L1210 tumors (*9*, *10*), Ehrlich ascites (*11*−*13*), and sarcoma 180 and P388 tumor lines (*14*). Although the exact mechanism of action of dirhodium compounds has not yet been elucidated, the most probable targets are DNA (*15*), RNA (*16*, *17*), and enzymes (*18*) involved in DNA and RNA synthesis. Studies of the binding affinity of $Rh_2(O_2CCH_3)_4$ to several biomolecules by employing ^{14}C-labeled $Rh_2(O_2CCH_3)_4$ indicated that $Rh_2(O_2CCH_3)_4$ is only slightly reactive toward native calf thymus DNA and polyguanylic (poly-G) and polycytidylic (poly-C) acids, but binds fairly well to denatured DNA and polyadenylic acid (poly-A) (*11*, *12*). The interactions of $Rh_2(O_2CCH_3)_4$ with adenine nucleos(t)ides (*11*, *12*, *19*, *20*) are established by axial binding of the adenine bases (via N7 and N1 if available (*19*)) and formation of hydrogen bonds between the exocyclic adenine NH_2 groups and the oxygen atoms of carboxylate ligands (for binding via N7), as evidenced by the reported crystal structures of $Rh_2(O_2CCH_3)_4(1\text{-}MeAdo)_2$[1] (*21*) and $[Rh_2(O_2CCH_3)_2(NHCOCF_3)_2(9\text{-methyladeninium})_2](NO_3)_2$ (*22*). In

---

[†] K.R.D. gratefully acknowledges the Welch Foundation (Grant A-1449) for financial support. The NMR instrumentation at the Biomolecular NMR Laboratory at Texas A&M University was supported by a grant from the National Science Foundation (DBI-9970232) and the Texas A&M University System.

* To whom correspondence should be addressed. E-mail: dunbar@mail.chem.tamu.edu. Phone: (979)-845-5235. Fax: (979)-845-7177.

[1] Abbreviations: Ado, adenosine; CD, circular dichroism; COSY, double-quantum-filtered correlation spectroscopy; dap, 1,12-diazaperylene; dsI, native d(CTCTCAACTTCC)·d(GGAAGTTGAGAG); dsII, metalated d(CTCTC*A*ACTTCC)·d(GGAAGTTGAGAG) (dsD); DTolF, anion of *N,N′-p*-tolylformamidinate; ESI-MS, electrospray ionization mass spectrometry; HPLC, high-performance liquid chromatography; HSQC, heteronuclear single-quantum correlation; MALDI-MS, matrix-assisted laser desorption ionization mass spectroscopy; NOESY, 2D nuclear Overhauser spectroscopy; ssI, native d(CTCTCAACTTCC); ssII, native d(GGAAGTTGAGAG); ssIII, metalated d(CTCTC*A*ACTTCC); T_m, melting temperature of a DNA duplex.

10.1021/bi701901c CCC: $40.75

the presence of DTolF groups, however, 9-ethyladenine (*23*, *24*) and d(ApA) (*25*) bind to the dirhodium unit $[Rh_2(DTolF)_2(CH_3CN)_6]^{2+}$ in a bridging fashion through positions N7 and N6 of the adenine bases. Furthermore, in the cytosine and 1-methylcytosine complexes with $Rh_2(HNOCCF_3)_4$, the pyrimidine ring binds axially to the dirhodium core via site(s) N3 or both N3 and O2, and the structure is further stabilized by intramolecular hydrogen bonds between the nucleobase exocyclic groups and the dirhodium trifluoroacetamidate moieties (*26*).

In spite of earlier claims (*11*, *12*), recent studies revealed that guanine nucleobases (*27*−*29*), guanine dinucleotides (*30*−*32*), and double-stranded DNA (*33*) also bind to dirhodium units, although the reactivity of $Rh_2(O_2CCH_3)_4$ is lower as compared to other dirhodium compounds (*33*, *34*). In two studies, the reactions of dirhodium(II) complexes with single-stranded oligonucleotides were monitored by mass spectrometry and enzymatic digestion studies (*35*, *36*). To gain further insight into the interactions of dirhodium complexes with DNA, we pursued the goal of structurally characterizing in solution a dirhodium−oligonucleotide duplex by 2D NMR spectroscopy. Herein, we report the structural characterization of the duplex d(CTCTC*A*ACTTCC)·d(GGAAGTTGAGAG) with the dirhodium cross-link at the C*A* site (dsII; C* and A* indicate the metalated sites). The interactions of the same duplex with the dirhodium complex *cis*-$[Rh_2(\mu\text{-}O_2CCH_3)_2(\eta^1\text{-}O_2CCH_3)(dap)(CH_3OH)](O_2CCH_3)$ containing the intercalating group dap have been the subject of another detailed NMR spectroscopic investigation (*37*).

EXPERIMENTAL PROCEDURES

Materials. The compound $Rh_2(O_2CCH_3)_4$ was prepared by standard procedures (*8*). The DNA oligonucleotide d(CTCTCAACTTCC) (ssI) and its complementary strand d(GGAAGTTGAGAG) (ssII) were purchased from Integrated DNA Technologies, Inc. (Coralville, IA) as crude materials. The enzymes Phosphodiesterase I (SVP) and II (BSP) were obtained from Sigma.

Oligonucleotide Purification. The crude oligonucleotide materials for ssI and ssII were purified by anion exchange HPLC chromatography. A Dionex DNAPac PA-100 (22 × 250 mm) anion exchange column was used on a Beckman Coulter System Gold instrument equipped with a 168 diode array detector for large-scale purification of oligonucleotides using the following elution conditions: 25 mM ammonium acetate in a CH_3CN/H_2O (10:90) solution (eluent A) and eluent A + 1.0 M NaCl (eluent B) starting with 28% eluent B, which was increased to 33% eluent B for 19 min to 60% eluent B for the next 18 min to 100% eluent B for the final 5 min with a 10 mL/min flow rate. The fractions collected from the HPLC purification were reduced in volume using a centrifugal evaporator (Jouan, Winchester, VA) and desalted on a Sephadex G-25 size exclusion column. The collected fractions from the size exclusion column were filtered through a 0.22 μm membrane (Fisher Scientific), and their concentrations were determined by UV spectroscopy (Shimadzu UV 1601PC spectrophotometer) at 260 nm prior to the samples being lyophilized.

Preparation and Isolation of the Metalated Duplex dsII. A solution of $Rh_2(O_2CCH_3)_4$ in H_2O was added to an oligonucleotide solution of d(CTCTCAACTTCC) (ssI) in H_2O in a 5:1 ratio (5 mM final concentration of oligonucleotide), the metal−DNA mixture was incubated at 37 °C for ∼4−5 h, and the progress of the reaction was monitored over time by anion exchange column HPLC (Figure S1a in the Supporting Information). The major adduct of the reaction (eluting at ∼22 min) was separated from the reaction mixture by anion exchange HPLC chromatography using a Dionex DNAPac PA-100 (9 × 250 mm) column. The same eluents used for the purification of the free oligonucleotides were used for the purification of the metalated adduct, with a gradient of 20−35% eluent B over a 30 min period and 35−100% eluent B over the next 20 min with a reduced flow rate of 3 mL/min. The collected fractions were desalted on a Sephadex G-25 size exclusion column and lyophilized. The dried and desalted major adduct from the anion exchange HPLC column (Figure S1a) was reinjected into a MetaChem Inertsil ODS-3 (10 × 250 mm) reversed-phase HPLC column and was further separated into several peaks, A−E (Figure S1c), under the following elution conditions: 25 mM ammonium acetate in H_2O (eluent A)/25 mM ammonium acetate in MeCN (eluent B) with a gradient of 5−10% eluent B over 10 min, 10−20% eluent B over the next 20 min, and finally 20−100% eluent B in the remaining 20 min. Samples were collected for the metalated species A−E (Figure S1c), and each metalated adduct was added to the complementary strand (ssII). The molecular mass of each single-stranded adduct A−E collected from the reversed-phase column is $[M + Rh_2(O_2CCH_3)_3]$, M = ssI, as determined by ESI-MS (Figure S2 in the Supporting Information).

The concentrations of the solutions of the single-stranded metalated species (Figure S1c) were estimated by measuring the absorbance at 260 mn. On the basis of the calculated concentrations, a quantity of the purified complementary strand d(GGAAGTTGAGAG) (ssII) was added to each metalated strand. The resulting solutions of the double-stranded adducts were injected into the anion exchange column under the same conditions employed for the isolation of the single-stranded adducts except for the gradient, which was 28−31% eluent B over a 6 min period, 31−55% eluent B over the next 10 min, and 55−100% B for the final 5 min (Figure S3 in the Supporting Information). The concentrations of the collected fractions dsA−dsE were measured by UV spectroscopy, and the samples were reduced in volume, desalted, and lyophilized. Typically, the color of the dirhodium samples was pink or light purple depending on the concentration of the adduct. As indicated by detailed NMR experiments, adduct dsD (dsII) exhibits the most prominent changes among the modified double-stranded oligonucleotides studied (dsA−dsE) and thus is the focus of this report.

NMR Experiments. The final sample of dsII was dissolved in a 40 mM $KHPO_4$ buffer solution (pH 6.9) containing 300 mM NaCl and 0.2 mM DSS, lyophilized twice with D_2O, and redissolved in 99.96% D_2O. For observation of the exchangeable protons, the dsI and dsII samples were dissolved in 90% H_2O/10% D_2O. The final concentration of each sample used for collection of the NMR data was 1 mM (duplex), and the volume was 260 μL in a Shigemi tube (Shigemi, Inc., Allison Park, PA). The 2D NMR data sets were collected at 15 °C. NMR experiments were performed on either a Varian Inova 500 MHz spectrometer equipped with a 5 mm indirect detection probe or a Varian 600 MHz spectrometer equipped with a triple-axis gradient pentaprobe. All chemical shifts were referenced to internal DSS (sodium 2,2-dimethyl-2-silapentane-5-sulfonate) (*38*). NOESY experiments in D_2O were performed by using a Varian pulse sequence (noesy.c 14.1) with a mixing time of 280 ms, a 10 ppm sweep width, in the hypercomplex mode, 2150 complex points, 512 t_1 blocks, 32−64 scans per t_1 block, 3 or 9 s delay times, and water suppression by presaturation during relaxation delay. 2D [$^1H-^1H$] DQF-COSY (double-quantum-filtered correlation spectroscopy) spectra were typically collected with a 10 ppm sweep width, 1792 data points in the t_2 dimension, 500 t_1 increments, and 32 scans per t_1 increment using the Varian dqcosy.c 14.1 pulse sequence. The chemical shifts of the imino and amino protons were assigned by collecting Watergate-NOESY spectra at 15 °C with a mixing time of 200 ms (*39*). The assignments of the H2 protons of the adenosine residues and the ^{13}C atoms of the aromatic rings were performed by a combination of short-range (one-bond) and long-range [^1H, ^{13}C] heteronuclear single-quantum correlation (HSQC) experiments (*40*). All 2D NMR data were processed using the program nmrPipe (*41*) with the 90° phase-shifted sine-bell apodization function and zero-filling. The baseline was corrected with first- and second-order polynomials. The program SPARKY (http://www.cgl.ucsf.edu/home/sparky/) was used for the peak assignments of dsI and dsII.

Enzyme Digestion Studies. Enzymatic digestion experiments were carried out using Phosphodiesterase I from *Crotallus adamanteus* venom (SVP) (3′ ↔ 5′ DNA exonuclease) and Phosphodiesterase II from bovine spleen (BSP) (5′ → 3′ DNA exonuclease). Phosphodiesterase I (SVP) digestions were performed at room temperature with no additional buffer using 5 times less enzyme than the incubations with Phosphodiesterase II (BSP) digestions, which were performed for 2 h at 37 °C with no additional buffer.

Mass Spectroscopy. Electrospray mass spectra of the isolated dirhodium adducts were acquired on an MDS Sciex API QStar Pulsar (Toronto, Ontario, Canada) fitted with a Protana (Odense, Denmark) nanoelectrospray source. All spectra were acquired in the negative ion mode in 50% H_2O and 50% 2-propanol with 5 mM ammonium acetate. The spray voltage was between −1050 and −1100 V. The nozzle-skimmer potential was set to −5 V to minimize fragmentation in that region.

Thermal Denaturation Experiments. The thermal melting profiles for dsI (unmetalated duplex) and dsII (metalated duplex) were obtained by monitoring the solutions at 260 nm on a CARY 300 Bio UV−vis spectrometer (Varian) equipped with a six-cell sample changer and temperature control. Capped 10 mm path length cuvettes were used, and one of the cuvettes was filled with buffer as a reference. The same salt and buffer conditions used for preparation of the NMR samples were used for the thermal denaturation experiments. Stock solutions of dsI and dsII were prepared at a concentration of 2 μM, and 900 μL of the stock solution was used for each measurement. The temperature was increased from 5 to 90 °C at a rate of 0.3 °C/min and then decreased to 5 °C for 5 min; the first derivative of each melting profile was used to calculate the melting temperatures T_m for dsI and dsII.

Circular Dichroism Spectropolarimetry. Circular dichroism (CD) spectropolarimetry was employed to investigate the average conformation of dsII. Data were collected on an AVIV 62DS spectropolarimeter. In a typical experiment, a 2 μM solution of duplex dissolved in the NMR buffer solution was added to a 10 mm cuvette, and the data were recorded between 200 and 350 nm with a bandwidth of 1 nm and an averaging time of 5 s.

Molecular Modeling. The sander program in Amber (*42*) (version 9) was used to minimize the manually docked dirhodium−DNA complex with the generalized Born solvation model and a nonbonding cutoff of 60.0 Å (Supporting Information). Unknown parameters and charges were developed on the basis of the X-ray crystal structure of dirhodium tetraacetate (*43*) and the TPSS (*44*) optimized complex *cis*-$[Rh_2(\mu\text{-}O_2CCH_3)_2(\eta^1\text{-}O_2CCH_3)(A\text{-}N7)(C\text{-}N4)(H_2O)]^+$ (Supporting Information). TPSS calculations with density-fitting basis sets (*45*) were performed using Gaussian 03 (*46*) with the 6-31G(d′) basis set (*47*) for C, N, O, and H and the all-electron DGDZVP basis set (*48*) for Rh. Force constants were set to reasonable values on the basis of similar terms in the ff03 force field. The new parameters were validated by comparing the modified ff03-optimized geometry of dirhodium tetraacetate with the crystal structure (*43*) and the modified ff03-optimized geometry of the dirhodium−DNA adduct with the TPSS-optimized *cis*-$[Rh_2(\mu\text{-}O_2CCH_3)_2(\eta^1\text{-}O_2CCH_3)(A\text{-}N7)(C\text{-}N4)(H_2O)]^+$ structure.

RESULTS

Determination of T_m. UV melting profiles were carried out to determine the distortion induced by the dirhodium binding in dsII as compared to the native DNA duplex (dsI). The T_m values of dsI and dsII, under identical experimental conditions, are 47.1 ± 1 and 24.2 ± 1 °C, respectively (Figure S4 in the Supporting Information). The decrease in the T_m value ($\Delta T_m = -22.9$ °C) for dsII indicates that the double-stranded oligonucleotide is considerably destabilized due to the metal binding and corroborates the presence of a covalent *intrastrand* dirhodium adduct (*49*).

CD Data. The circular dichroism spectrum of dsII exhibits a slight shift of the apex point as compared to that of dsI (Figure S5 in the Supporting Information), which indicates that the overall conformation of dsII is similar to that of dsI (B-DNA).

Enzyme Digestion Studies. Exonuclease digestions followed by MS studies were performed on a sample of ssIII (single-stranded adduct D), which has the formula $[M + Rh_2(O_2CCH_3)_3]$, M = ssI, as determined by ESI-MS (Figure S2), before the enzyme digestions. The successive cleavage of nucleotides by both Phosphodiesterases I and II from the 3′ and 5′ ends of ssIII (single-stranded adduct D), respectively, is inhibited at the A6 and C5 residues (Figure S6 in the Supporting Information), which strongly supports dirhodium binding to these sites (*50*−*52*) and corroborates the conclusions from the 2D NMR investigation of dsII.

NMR Characterization of dsI. The combined use of NOESY and DQF-COSY experiments allowed the assignment of the protons for dsI (Chart 2), which was performed by standard procedures based on the proximity of the sugar protons H1′, H2′, H2″, and H3′ to the protons on the same and the 3′-adjacent residues in a typical B-DNA conformation

Table 1: ^{1}H NMR Chemical Shifts (ppm) of the Protons in the Dirhodium Adduct dsII at 15 °C[a,b]

Base	H6/H8	H2/H5/Me	H1′	H2′	H2″	H3′	H4′	H5′	H5″	N4Hb/N4He[c]	GH1/TH3
C1	7.92	5.94	5.87	2.28	2.59	4.65	4.11	3.80	3.86	7.77/7.19	
T2	7.67	1.67	6.19	2.29	2.59	4.90	4.29				13.88 (−0.09)
C3	7.66	5.66	6.08	2.18	2.54	4.81	4.19			8.36 (0.09)/7.13	
T4	7.36	1.56	6.16 (0.20)	2.05	2.24 (0.19)	4.81	4.24		4.07		*d*
C5*[i]	7.93 (0.44)	6.23 (0.56)	5.70 (0.54)	2.42 (0.44)	2.47 (0.25)	4.44 (−0.35)	4.21 (0.17)	4.07		8.76 (0.19)[e]	
A6*[i]	8.74 (0.55)	7.17	6.16 (0.30)	2.75	2.99	5.02	4.40	4.12	4.08		
A7	8.29 (0.17)	7.79 (0.22)	6.23 (0.19)	2.67	2.89	5.03	4.52		4.25		
C8	7.26	5.15	5.78	1.97	2.50	4.67	4.24			7.86 (0.12)/6.65	
T9	7.44	1.48	6.08	2.18	2.59	4.88	4.20	4.11	4.11		14.10
T10	7.47	1.65	6.12	2.20	2.56	4.88	4.23				13.84 (−0.07)
C11	7.64	5.77	6.08	2.28	2.48	4.87	4.21			8.52/7.04	
C12	7.74 (0.20)	5.87 (0.28)	6.22	2.30	*f*	4.56	4.18 (0.19)	4.07	4.07	*g*	
G13	*f*		5.59	2.40	2.53	4.76	4.13	3.62			*g*
G14	7.85		5.35	2.66	2.71	4.97	4.31	4.08	4.00		12.81 (−0.02)
A15	8.14	7.37	5.94	2.71	2.91	5.07	4.44	4.20	4.12		
A16	8.01	7.53	6.06	2.63	2.89	5.05	4.47		4.24		
G17	7.38		5.77	2.41	2.65	4.84	4.40				12.73 (−0.09)
T18	7.22	1.12	6.08	2.13	2.58	4.83	4.29	4.23	4.16		13.87 (0.03)
T19	7.32	1.56	*f*	*f*	*f*	4.89	4.20				13.11 (−0.67)
G20	*h*		5.47	2.30	2.48	*h*	*h*				11.19 (−1.38)
A21	8.09	7.67	5.85	2.66	2.71	5.00	4.37				
G22	7.75		5.47	2.53	2.65	4.97	4.32				12.60 (−0.09)
A23	8.06	7.83	6.13	2.62	2.89	5.01	4.42		4.13		
G24	7.65		6.00	2.25	2.42	4.63	4.15	4.11			*g*

[a] The acetate resonances for *a*CH_3, *b*CH_3, *c*CH_3 of the dirhodium unit appear at 1.77, 1.93, and 1.99 ppm, respectively. [b] Numbers in parentheses indicate the difference between the chemical shift of the dirhodium adduct dsII and the unmodified duplex dsI resonance [$\Delta\delta = \delta(\text{dsII}) - \delta(\text{dsI})$]; the $\Delta\delta$ values for the nonexchangeable protons are listed if $|\Delta\delta| \geq 0.15$. The other $\Delta\delta$ values are omitted for the sake of simplicity. Positive and negative values of $\Delta\delta$ indicate downfield and upfield shifts, respectively. [c] N4Hb and N4He are the cytosine hydrogen-bonded and exposed amino protons. [d] Thymine imino proton not detected. [e] N4He of C5* is displaced due to metal binding. [f] Proton not detected due to weak or overlapped cross-peaks. [g] Imino and amino protons of frayed terminal bases not detected (*74*). [h] Proton not detected due to lack of stacking (*58*, *69*) and flexibility (*71*, *100*) or fast conformational exchange (*72*, *73*) of the base. [i] The asterisk denotes the residues binding to the dirhodium core.

Chart 2: Sequential Numbering Scheme for dsI

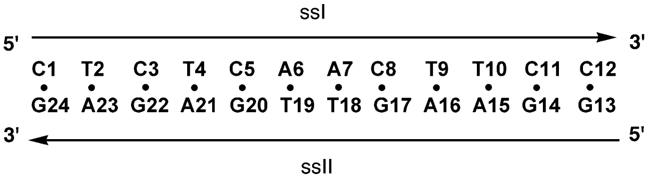

(*53*) (Figures S7−S10 in the Supporting Information); the values for the chemical shifts of the protons are listed in Table S1 in the Supporting Information. An intense cross-peak between the H2 protons of residues A6 and A7 (Figure S8) indicates that the duplex dsI is in the B-DNA conformation (*53*).

NMR Spectroscopic Data for dsII. Assignment of Nonexchangeable Protons. NOESY, DQF-COSY, and HSQC spectra were collected and analyzed to assign the resonances for the nonexchangeable protons of dsII. The cross-peaks between the cytosine protons H5 and H6 for dsII were readily identified by their presence in the DQF-COSY spectrum (Figure S11 in the Supporting Information) (*54*). The chemical shifts of the protons for dsII and the notable changes as compared to the corresponding protons in dsI are listed in Table 1. A global indication of the localization of the structural distortions in dsII is derived by comparing the chemical shifts for the nonexchangeable protons of dsI to those of dsII; these changes are summarized in the graph (Figure 1).

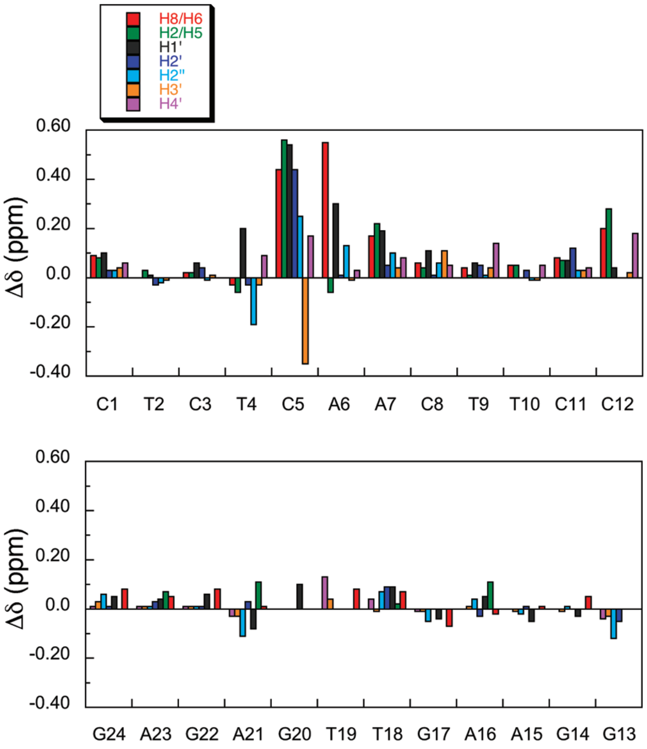

FIGURE 1: Differences in the chemical shifts of the nonexchangeable protons upon binding to the dirhodium unit [$\Delta\delta = \delta(\text{dsII}) - \delta(\text{dsI})$]. Bars in the positive and negative regions indicate downfield and upfield shifts, respectively.

In regards to the aromatic protons of the dsII bases, the resonance for A6H8 exhibits a substantial downfield shift of $\Delta\delta = +0.55$ ppm (Table 1, Figures 1 and 2) as compared to that of A6H8 for dsI (Figure S7), which indicates that the binding of the dirhodium unit takes place at site N7 of the A6 residue. Comparable downfield shifts of the H8 resonance of adenosine ($\Delta\delta \approx +0.55$ ppm) have been recorded in its complex with dirhodium tetraacetate (*55*). In the case of the

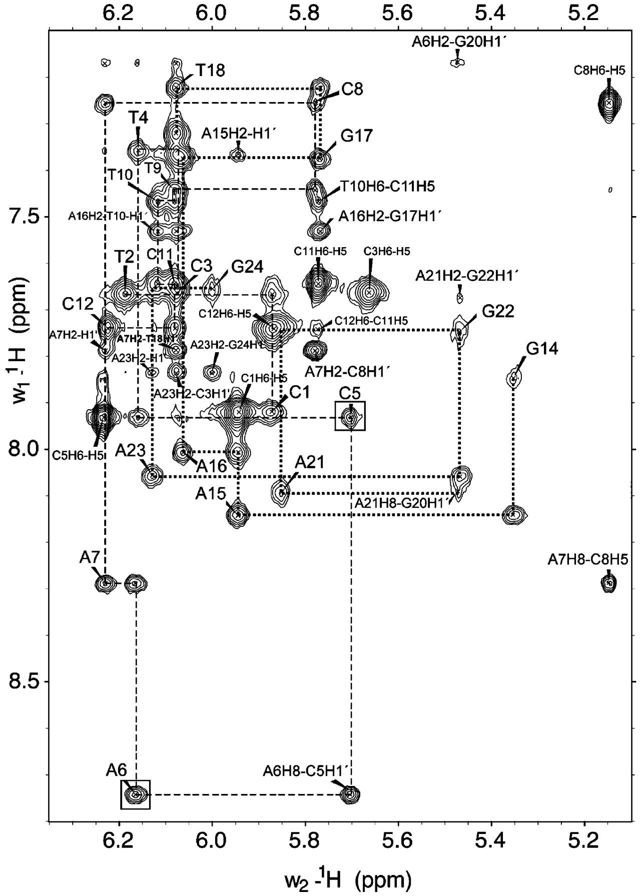

FIGURE 2: Contour plots of the NOESY spectrum for duplex dsII in D$_2$O (collected at 15 °C, 280 ms mixing time) exhibiting the correlation between the aromatic protons of the bases and the H1′ protons of the sugar rings.

interaction of the duplex dsI with the dirhodium complex *cis*-[Rh$_2$(μ-O$_2$CCH$_3$)$_2$(η^1-O$_2$CCH$_3$)(dap)(CH$_3$OH)](O$_2$CCH$_3$) containing the intercalating group dap (dap = 1,12-diazaperylene), binding also takes place via site N7 of A6, but the downfield shift of A6H8 ($\Delta\delta$ = +0.14 ppm) is counterbalanced by the upfield shift of the resonances due to the intercalation of the dap group between residues A6 and A7 (*37*). Considerable downfield shifts of the H8 purine resonances of DNA oligonucleotides have also been recorded in platinum−DNA adducts, wherein the metal binds to the N7 sites of the guanine residues (*56*−*58*).

In the duplex dsII, notable changes for residue C5 are the $\Delta\delta$ = +0.56 and +0.44 ppm downfield shifts of the H5 and H6 resonances, respectively, as compared to those of the corresponding protons in dsI. Additionally, the resonances of the deoxyribose protons H1′, H2′, H2″, and H4′ for residue C5 shift downfield by +0.54, +0.44, +0.25, and +0.17 ppm, respectively, whereas that of H3′ moves upfield by $\Delta\delta$ = −0.35 ppm as compared to those of dsI (Table 1). These appreciable chemical shift changes indicate that the C5 residue is bound to the dirhodium unit, inducing considerable structural changes to C5 of dsII. The downfield shifts of the H1′, H2′, H2″, and H4′ sugar protons of C5 (Figure 1) indicate that most likely the C5 residue deoxyribose ring is close to the dirhodium unit, resulting in metal-induced downfield shifts of the protons (*59*). The upfield shift of the C5H3′ sugar proton may be mainly attributed to the neighboring base diamagnetic ring current anisotropy (*60*). The substantial downfield shifts of C5H5 and C5H6 strongly suggest that the exocyclic site N4 of C5 is binding to the rhodium atom (*61*−*63*). In particular, characteristic downfield shifts of the C5H5 resonance (*63*−*66*) indicate the presence of the *anti* rotamer (*67*, *68*) of the base with respect to N3 in its metal-stabilized rare iminooxo form (Chart 3, vide infra).

Chart 3: Neutral and Metal-Stabilized Rare Cytidine Tautomers

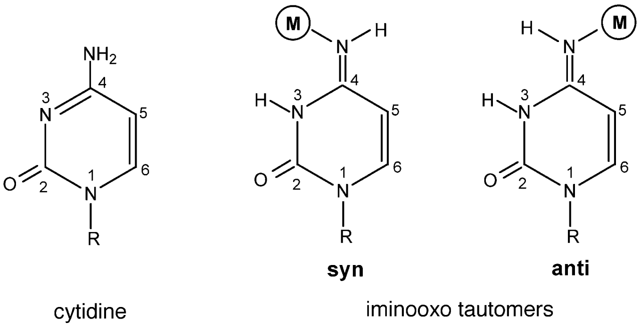

For dsII, the sequential contacts that give rise to intra- and internucleotide (nH1′−(n + 1)H6/H8) NOEs involving base H6/H8 to deoxyribose H1′ protons are observed for all the bases, but are absent in the complementary strand opposing the metal lesion site; e.g., the cross-peaks T19H6−H1′, T19H1′−G20H8, and G20H8−H1′ are absent, and G20H1′−A21H8 is weak (Figure 2). This is an indication of distortion of the stacking interactions between T19 and G20 (*58*, *69*, *70*). Moreover, the absence of any NOE contacts for G20H8 (complementary to C5*) is attributed to reduced stacking (*58*, *69*), which results in dynamic behavior or fast conformational exchange (flexibility) of this base on an intermediate NMR time scale (*69*−*73*). The aromatic−H1′ NOE cross-peaks for the bases C1, C12, and G13 are also missing (Figure 2), most likely due to terminal fraying effects (the changes in the chemical shifts of the C12 residue protons (Table 1) are attributed to fraying effects (*74*, *75*)). The NOE cross-peaks between T4H6 and C5H6, T4H6 and C5H5, and C5H6 and A6H8, which are the bases binding to the dirhodium unit or flanking the binding sites, are very weak or absent in the NOESY spectrum, indicating that the stacking between the aforementioned bases in dsII has been disrupted as compared to that in dsI (*58*, *69*). The intense cross-peak between the H2 protons of residues A6 and A7, however, indicates that the metalated duplex dsII in the 3′ direction of the lesion site remains in the B-DNA conformation (*53*).

The H2 protons of the adenine bases for dsI and dsII were assigned by performing long- and short-range HSQC and NOESY spectra. In the lr-HSQC spectra (Figure S12, top, in the Supporting Information), three-bond correlations are detected through cross-peaks between the H2 protons of adenine bases and the ^{13}C4 and ^{13}C6 carbon atoms in the respective aromatic rings. In the sr-HSQC spectra (Figure S12, bottom), one-bond correlations are detected, through cross-peaks between the H2 protons and the ^{13}C2 carbon atoms. In the sr-HSQC spectrum of dsII (Figure S12, bottom, right), all six H2 protons were identified except for partial overlap between A23H2 and A7H2; the two protons were rather easily identified in the corresponding NOESY spectrum by the correlation peaks with other protons (Figure 2). Overall, there were small changes in the chemical shifts of the carbon atoms of adenine bases for dsII; the resonances

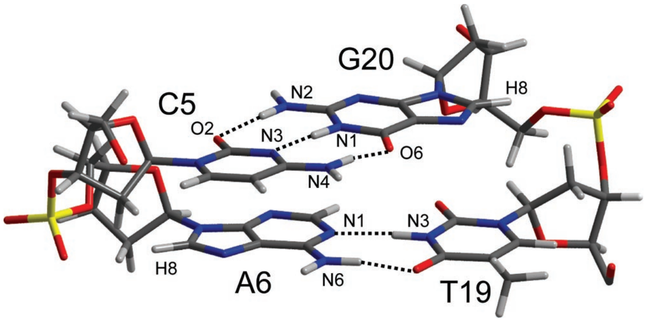

FIGURE 3: Watson−Crick hydrogen bonding between the partner bases C5 and G20 and A6 and T19 in dsI.

of the H2 protons, however, were downfield shifted by 0.1−0.2 ppm, except for A6H2, which exhibited a ~0.1 ppm upfield shift (Table 1, Figure 1).

The intraresidue NOE cross-peaks between the base H8/H6 protons and the sugar H1′ protons of dsII (except for bases T19 and G20, for which these cross-peaks are missing, Figure 2) are weaker than those detected between the cytosine atoms H5 and H6, e.g., C3, C5, C8, and C11 (Figure 2), which indicates that the H8/H6 to H1′ distances for the bases are longer than the fixed length of 2.4 Å between H5 and H6 in cytosine (*53*), establishing that in dsII each base adopts an *anti* conformation about its glycosyl bond (*74*). Moreover, the intensities of the C5H6−H3′ and A6H8−H3′ cross-peaks in the NOESY spectrum of dsII, when examined qualitatively, are comparable in intensity to the aromatic−H3′ cross-peaks for the other bases of the duplex, indicating that the deoxyribose rings at the metal binding site are S-type (*56*, *57*) as in B-DNA.

Assignment of the Exchangeable Protons. Watergate-NOESY spectra in H_2O/D_2O (90:10) were collected to assign the exchangeable protons of dsII. Characteristic features of the G•C base pair Watson−Crick hydrogen bonding in double-stranded DNA (Figure 3) are the cross-peaks between both the N4Hb (hydrogen-bonded) and N4He (exposed) amino protons of the cytosine base and the N1H imino proton of the partner guanine base (Figure 4, top; e.g., C3N4He−G22N1H, C3N4Hb−G22N1H, C5N4He−G20N1H, C5N4Hb−G20N1H, C8N4He−G17N1H, C8N4Hb−G17N1H) (*74*). In dsI, both amino protons of each cytosine residue give NOE cross-peaks with the H5 resonance of the same base except for the terminal residues (Figure S13, top, in the Supporting Information), and thus, the guanine N1H resonances are linked to the backbone cytosine protons. In the case of dsII, however, for residue C5, only the C5H5−N4Hb cross-peak is observed (Figure S13, bottom) as opposed to the presence of both C5H5−N4Hb and C5H5−N4He cross-peaks for dsI (Figure S13, top). Moreover, the N1H proton of G20 has a cross-peak with C5N4Hb only, but not with C5N4He (Figure 4, bottom). The previous findings imply that one of the exocyclic amino group protons of C5 has been displaced, due to the dirhodium binding to site N4 of the C5 residue (*68*). The resonance for C5N4Hb in dsII is downfield shifted by $\Delta\delta = +0.19$ ppm as compared to that of dsI and appears at 8.76 ppm (Table 1), which is essentially the downfield extreme of the typical range for hydrogen-bonded exocyclic amino protons (6.6−9.0 ppm) (*53*). The cross-peak between G20N1H and C5N4Hb (Figure 4, bottom) implies that C5 and G20 are still close to each other. As indicated earlier, the metal adopts an *anti* orientation with respect to N3, which is required for base C5 to remain close to G20. The considerable downfield shift of the C5 amino proton N4Hb ($\Delta\delta = +0.19$ ppm) is attributed to the inductive effect of the metal binding at the N4 site (*63*, *76*) or may reflect a decrease in the extent of stacking interactions involving C5 (*74*, *77*). In the 3′ direction of the lesion site, both the base pair cytosine N4H−guanine N1H partner cross-peaks are observed (e.g., C8N4Hb−G17N1H, C8N4He−G17N1H, C11N4Hb−G14N1H, C11N4He−G14N1H), although weaker than in dsI. In contrast, in the 5′ direction of the lesion site, the C3N4Hb−G22N1H and C3N4He−G22N1H cross-peaks are absent (Figure 4, bottom), although both C3 amino protons were found to have NOE cross-peaks to the H5 proton of the same base (Figure S13, bottom); this indicates that the Watson−Crick hydrogen bonding in C3•G22, which is two base pairs away from the lesion site in the 5′ direction, is destabilized (*58*, *74*, *78*).

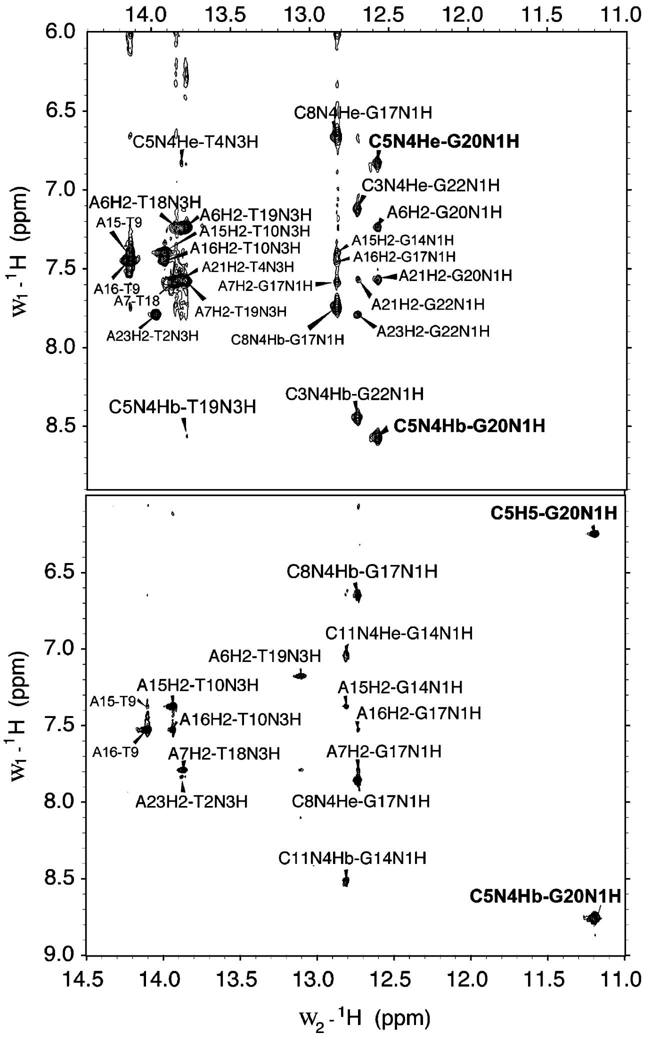

FIGURE 4: Contour plots of the Watergate-NOESY spectra (collected at 15 °C, 200 ms mixing time) of duplexes dsI (top panel) and dsII (bottom panel) showing NOE correlations between the imino and amino protons.

The N1H imino protons of the guanine and the N3H imino protons of the thymine residues participate in Watson−Crick hydrogen bonding in native DNA (Figure 3, G•C and A•T pairs, respectively) and appear in the range 12.0−14.5 ppm for dsI (Figure 5, top; Table S1). In general, the imino protons of dsII exhibit moderate upfield shifts (−0.1 ppm) as compared to the resonances for the corresponding imino

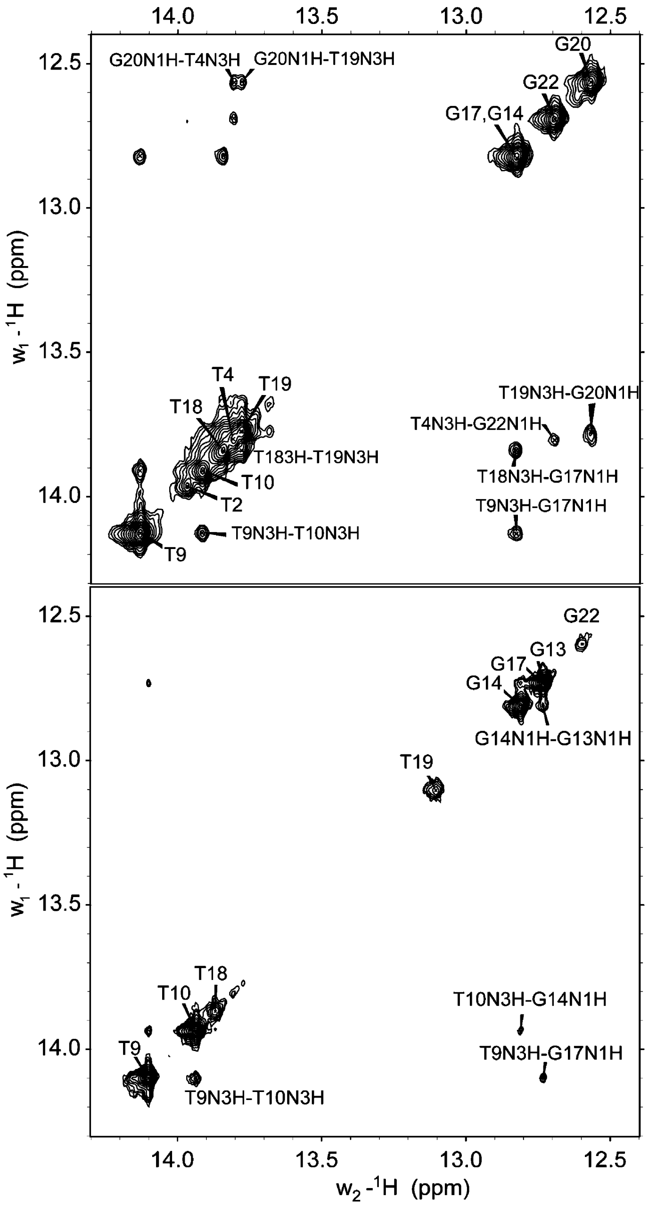

FIGURE 5: Contour plots of the Watergate-NOESY spectra (collected at 15 °C, 200 ms mixing time) of duplexes dsI (top panel) and dsII (bottom panel) showing the imino−imino proton NOE correlations. For dsII, G20N1H is further upfield from the region shown.

protons of dsI, except for the substantial upfield shifts in the resonances of the imino protons for T19N3H ($\Delta\delta = -0.67$ ppm) and G20N1H ($\Delta\delta = -1.38$ ppm) (Figure 4, bottom; Table 1), which are the partner bases to the binding sites in dsI (Figure 3). The substantial upfield shift of T19N3H indicates weakening of the hydrogen bonds to A6 and in the case of G20N1H complete disruption of G20N1H−C5N3 (Figure 3); the latter is supported by the value of $\delta = +11.2$ ppm for G20N1H (*74*, *77*, *79*, *80*) and the broadness of the G20N1H resonance at 2 °C in 90% H_2O/10% D_2O (*78*,*81*), although substantially upfield-shifted imino guanine protons have been recorded in spite of the protons being involved in hydrogen bonding (*82*).

As expected for dsI, the nonterminal imino protons exhibit NOE cross-peaks to the neighboring imino protons in the same strand (Figure 5, top; e.g., T9N3H−T10N3H, G17N1H−T18N3H, T19N3H−G20N1H) as well as to the imino protons in the adjacent base pairs (e.g., T4N3H−G20N1H and T4N3H−G22N1H in the 3′ and 5′ directions, respectively, and T9N3H−G17N1H). In the case of dsII, however, the pattern of connectivities for the imino protons is disrupted in the 5′ direction of the lesion site; e.g., T4N3H−G20N1H, T4N3H−G22N1H, and T19N3H−G20N1H are absent (Figure 5, bottom). The G17N1H−T18N3H cross-peak is absent, and the T9N3H−G17N1H cross-peak is much weaker than in dsI.

Evidence of Watson−Crick hydrogen bonding between DNA complementary strands also stems from the correlation peaks between the H2 proton of the adenine residue and the N3H imino protons of the thymine residue in the same base pair and the adjacent ones (Figure 4, top; e.g., A6H2−T19N3H, A6H2−T18N3H, A7H2−T19N3H, A15H2−T9N3H, A16H2−T9N3H, A16H2−T10N3H, A21H2−T4N3H) as well as to the adjacent guanine N1H imino protons, e.g., A15H2−G14N1H, A16H2−G17N1H, A21H2−G20N1H, A21H2−G22N1H, A23H2−G22N1H, A6H2−G20N1H, A7H2−G17N1H (*53*). For dsII (Figure 4, bottom), the correlation peaks for the base pairs A6H2−T19N3H and A7H2−T18N3H are observed, although much weaker, but A6H2−T18N3H, A7H2−T19N3H, A6H2−G20N1H, A21H2−G22N1H, and A23H2−G22N1H between neighboring base pairs and A21H2−T4N3H between partner bases are absent (A23H2−T2N3H is weak). On the contrary, the A15H2−T10N3H, A16H2−T10N3H, A15H2−T9N3H, A16H2−T9N3H, A15H2−G14N1H, and A16H2−G17N1H correlations for the bases in the 3′ direction of the lesion site are observed, although weaker than in dsI (Figure 4, bottom). The previous findings suggest that the base stacking and the hydrogen bonding are considerably disrupted in the 5′ direction of the lesion site, which corroborates the absence of the imino−imino correlation peaks in the same direction (vide supra).

Dirhodium Unit Acetate Groups. As indicated by the mass spectum of ssIII (Figure S2, adduct D) and the acetate region of the NOESY spectrum for dsII (Figure S14 in the Supporting Information), only three acetate groups remain attached on the dirhodium core in dsII. The acetate groups on the dirhodium unit of dsII, referred to as aCH$_3$, bCH$_3$, and cCH$_3$, resonate at 1.77, 1.93, and 1.99 ppm, respectively (the acetate groups in $Rh_2(O_2CCH_3)_4$ resonate at 1.89 ppm in D_2O). The different chemical shifts of the three dirhodium acetate groups in dsII indicate that, as expected, they are not equivalent. On the basis of the values of their chemical shifts for dsII, the bCH$_3$ and cCH$_3$ groups are bridging the dirhodium core and aCH$_3$ is monodentate. The previous NMR assignments are supported by the chemical shifts of acetate groups in dirhodium compounds with one dangling and two bridging acetate groups; typically, the monodentate groups resonate upfield (~1.7 ppm) from the bridging acetate ligands (*83*, *84*). The presence of a monodentate acetate group in dsII is also corroborated by the modeling studies (steric reasons). For dsII, an NOE cross-peak is observed between acetate bCH$_3$ and A6H8 (Figure S14), which is one of the binding residues. The monodentate acetate group aCH$_3$ exhibits NOE cross-peaks to C3H6 and T4H6 in the 5′ direction of the lesion site, and the bridging group cCH$_3$ to T18H1′, T18CH$_3$, and G17H8 in the 3′ direction of the lesion site (Figure S14); these cross-peaks indicate that the acetate group aCH$_3$ is directed toward the 5′ end of ssI, whereas the acetate group cCH$_3$ is situated toward the 5′ end of the complementary strand ssII (Figure 6).

DISCUSSION

The structural characterization of the duplex d(CTCTC*A*ACTTCC)·d(GGAAGTTGAGAG) with the dirhodium lesion site indicates that considerable distortions are induced to the DNA structure upon binding to the metal, especially at the base pairs located at and near the binding sites, but the global conformation of dsII appears to be mainly that of dsI, i.e., B-DNA. This is supported by the CD data of dsII, the intense cross-peak between the H2 protons of the dsII residues A6 and A7 (*53*), and the NOE proton connectivity pattern along the two strands of the modified duplex (*53*, *74*), except for bases T19 and G20, which are the partner bases to the metal binding sites. The considerable downfield shifts of the aromatic proton resonances for C5 and A6 ($\Delta\delta \approx 0.5$ ppm) of dsII relative to dsI are consistent with the helix being right-handed, as usually observed for GG intrastrand cisplatin DNA duplexes (*85*). The duplex dsII, however, has been considerably destabilized as indicated by the substantial decrease in the melting temperature by $\Delta T_m = -22.9$ °C, as compared to dsI. The reduced thermal stability of dsII is attributed to the decreased stacking of the bases and the complete disruption and/or weakening of the hydrogen bonds within the base pairs (*86*−*88*) due to metal binding (vide infra). The decrease in the T_m value for dsII ($\Delta T_m = -22.9$ °C) suggests the presence of a covalent *intrastrand* dirhodium adduct (*49*), which is corroborated by the NMR data. The formation of intrastrand cisplatin cross-linked adducts at GG sites in various DNA sequences induces a decrease in the melting temperatures of the host duplexes by $\Delta T_m = 15-27$ °C (*88*), which is comparable to that for the dirhodium adduct dsII. When the duplex dsI binds to the dirhodium unit *cis*-$[Rh_2(\mu\text{-}O_2CCH_3)_2(dap)]^{2+}$, the net decrease in the melting point of dsI is considerably smaller ($\Delta T_m = -6.0$ °C) due to intercalation of the dap group between residues A6 and A7, apart from covalent binding of the A6 residue to the metal via N7 (*37*).

The halt of the Phosphodiesterases I and II at the A6 and C5 residues of ssIII, respectively (Figure S6), strongly supports dirhodium binding to these bases. The large downfield shift of A6H8 ($\Delta\delta = +0.55$ ppm, Table 1), which is comparable to that of the H8 resonance of adenosine ($\Delta\delta \approx +0.55$ ppm) in its complex with dirhodium tetraacetate (*55*), is attributed to the inductive effect of the metal (*89*) and indicates that site N7 of the A6 residue is binding to the dirhodium unit (Figure 6). In the case of the duplex dsI with the dirhodium complex *cis*-$[Rh_2(\mu\text{-}O_2CCH_3)_2(\eta^1\text{-}O_2CCH_3)(dap)(CH_3OH)](O_2CCH_3)$, binding takes place via site N7 of A6 and the dap group intercalates between residues A6 and A7 (*37*). Apparently, for the given DNA sequence, site A6N7 is the preferable binding site in the presence (*37*) or absence (present study) of intercalation. In the crystal structure of dirhodium tetraacetate with tRNA^{phe}, however, axial binding of the A36 base takes place via site N1 (*90*), but in the case of dsII, the change in the chemical shift of A6H2 is negligible (Table 1), thus excluding N1 binding for base A6.

In the present dirhodium adduct dsII, C5 is the other base that establishes a coordination bond with the dirhodium unit (Figure 6). This is strongly supported by the enzyme digestion data, as well as by the considerable changes of the chemical shifts for the protons of C5 (Table 1). Although cytosine has a number of potential binding sites for the metal (Chart 3; e.g., N3, O2, N3/O2, N3/N4 (*91*)), metal binding to N7 of A6, which is in the major groove of DNA, and the substantial downfield shift of C5H5 ($\Delta\delta = +0.56$ ppm) (*61*−*63*) render the C5 exocyclic amino group N4, also located in the major groove (*92*), the suggested cytosine binding site of the dirhodium unit (Figure 6). Characteristic downfield shifts of the C5H5 resonance are typical of the *anti* cytosine rotamer (with respect to N3) in its metal-stabilized rare iminooxo form (Chart 3) (*64*−*66*); e.g., for the platinum complex *trans*-$[Pt(NH_3)_2(1\text{-}MeC\text{-}N4)_2](NO_3)_2$, downfield shifts of ∼0.5−0.7 ppm are observed for the cytosine H5 protons of the *anti*/*anti* rotamers (*63*). These appreciable downfield shifts of the cytosine resonances are attributed to the magnetic anisotropy of the d^8 Pt(II) atom in a square planar arrangement, which deshields protons situated directly above or below the coordination plane (*63*). The presence of the *anti* rotamer of cytosine is corroborated by the cross-peak between the N1H proton of G20 and C5N4Hb (Figure 4, bottom), which indicates close proximity of C5N4Hb and G20N1H in dsII (4.3 Å in the model, Figure 7), although Watson−Crick hydrogen bonding between G20 and C5 is disrupted (e.g., in the model for dsII, G20O6−C5N4Hb = 6.5 Å and G20N2H−C5O2 = 5.2 Å, and the partner bases G20/C5 are no longer coplanar, Figure 7); this is supported by the significant upfield shift of the imino proton G20N1H resonance ($\Delta\delta = -1.38$ ppm), the value of its chemical shift ($\delta = +11.2$ ppm, Table 1) (*74*, *77*−*80*), and its broadness in 90% H_2O/10% D_2O at 2 °C (*78*, *81*). On the other hand, the resonance for C5N4Hb in dsII is downfield shifted by $\Delta\delta = +0.19$ ppm as compared to that in dsI and appears at 8.76 ppm (Table 1), which is essentially the downfield extreme of the typical range for hydrogen-bonded exocyclic amino protons (6.6−9.0 ppm) (*53*). The considerable downfield shift of the C5 amino proton N4Hb ($\Delta\delta = +0.19$ ppm), however, is not due to G20O6−C5N4Hb hydrogen bonding (Figure 3), but rather is attributed to the inductive effect of the metal binding at the N4 site (*63*, *76*); e.g., the chemical shifts of the N4 exocyclic amino protons are downfield

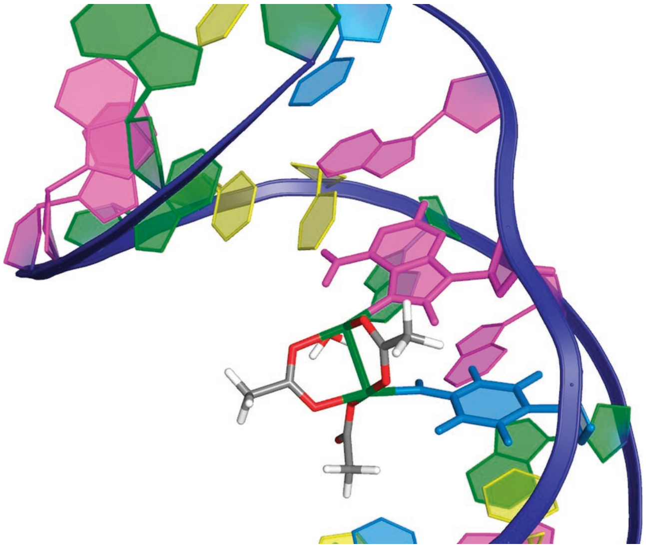

FIGURE 6: Model of dsII depicting the binding sites (C5N4 and A6N7) of the dirhodium unit *cis*-$[Rh_2(\mu\text{-}O_2CCH_3)_2(\eta^1\text{-}O_2CCH_3)]^+$. DNA base colors: A, pink; C, light blue; G, green; T, yellow. Blue ribbon = phosphodiester backbone. Atom colors: Rh, green; O, red; C, gray; H, white.

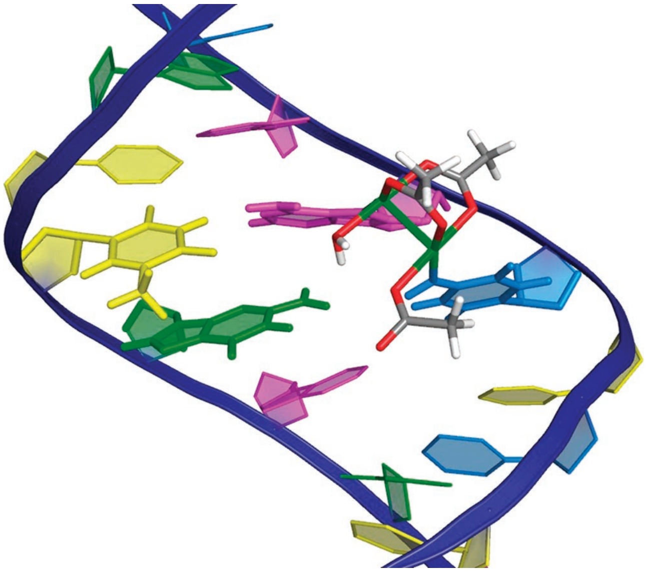

FIGURE 7: Model of dsII depicting the partner bases C5•G20 and A6•T19 and the bases C5 and A6 binding to the dirhodium unit *cis*-$[Rh_2(\mu\text{-}O_2CCH_3)_2(\eta^1\text{-}O_2CCH_3)]^+$. DNA base colors: A, pink; C, light blue; G, green; T, yellow. Blue ribbon = phosphodiester backbone. Atom colors: Rh, green; O, red; C, gray; H, white.

shifted by ∼1.2 ppm for the isomers of the platinum complex *trans*-$[Pt(NH_3)_2(1\text{-MeC-}N4)_2](NO_3)_2$ as compared to free cytosine (spectra collected in DMSO-d_6) (*63*, *76*). The metalation of the exocyclic amino group N4 of cytosine is known to stabilize the rare iminooxo form of the base and induce protonation of site N3 (Chart 3; protonation of C5N3H inhibits formation of the G20N1H−C5N3 hydrogen bond, Figures 3 and 7) (*68*, *91*), thus leading to rare nucleobase tautomers.

A theoretical study that has been performed on N4-metalated cytosine with Hg(I) and Pt(II) showed that the metalation of the amino group of the nucleobases improves the protonation energy of the nucleobase aromatic ring by 10−14 and 30−34 kcal/mol, respectively (*93*). Protonation of site N3 of cytosine, which is induced by metalation of N4, may lead to stabilization of mispairs such as a CH^+•G Hoogsteen base pair or a G^-•CH^+ ion pair, with significant biological consequences (*68*, *93*). In the case of the dirhodium adduct dsII, however, the CH^+•G Hoogsteen base pair (*94*) is ruled out due to the presence of the NOE cross-peak between G20N1H and C5N4Hb (Figure 4, bottom), and a G^-•CH^+ ion pair is not considered because G20N1H continues to be protonated at the pH of the 2D NMR data collection. The observation of G20N1H cross-peaks, although this proton is not hydrogen bonded, is consistent with slow exchange on the NMR time scale or minimal exposure to the solvent (*74*, *95*), most likely due to shielding from the minor groove by G20(NH2) (Figure 7). It is notable that the rate of exchange of the GN1H imino proton has been correlated to the relative position of the kink (bend) of the helix with respect to the G base (*96*−*98*).

The conformational changes and the Watson−Crick hydrogen-bonding disruption of the C5•G20 base pair are also indicated by the absence of the G20N1H−A6H2 NOE cross-peak (Figure 4), as opposed to the 3′ flanking base pair A6•T19, which still retains hydrogen bonding, albeit significantly weaker than in dsI, on the basis of the substantial upfield shift in the chemical shift of the imino proton T19N3H ($\Delta\delta = -0.67$ ppm, Table 1) and the intensity of the cross-peak A6H2−T19N3H (Figure 4, bottom) (*74*, *77*). The absence of T19H1′−G20H8 and G20H8−H1′ (Figure 2) and the imino T19N3H−G20N1H (Figure 5, bottom) and the weak G20H1′−A21H8 cross-peaks suggest disruption of the stacking interactions among T19, G20, and A21 (*58*, *69*), which together with the absence of any NOE contacts for G20H8 (*95*) corroborate high flexibility of residue G20 (*69*−*73*). Lack of the sequential *n*H1′−(*n* + 1)H6/H8 NOE cross-peaks at the C16−C17 and C17−G18 steps of the d(GCCG*G*ATCGC)•d(GCGATC-CGGC) duplex bearing a cisplatin unit cross-linking the two G* bases is attributed to an unusual position of C17 with respect to both its neighbors; i.e., the G4*−C17 base pair slides back and forth along a vector perpendicular to the local helix axis (*99*, *100*). Furthermore, the substantial downfield chemical shifts of the deoxyribose protons H1′, H2′, H2″, and H4′ (+0.54, +0.44, +0.25, and +0.17 ppm, respectively) for the partner base C5 (Table 1) indicate that the C5 deoxyribose ring may be close to the dirhodium unit (*59*), whereas the upfield shift of the C5H3′ sugar proton may be attributed to its positioning in the shielding cone of residue A6 (*100*); the absence (or weakness) of the NOE cross-peaks between the aromatic protons for T4, C5, and A6 and the missing contacts A6H2−T18N3H and A7H2−T19N3H indicate that stacking interactions are disrupted for T4, C5, and A6 as well (*58*, *69*). The hydrogen bonding for the base pairs T4•A21 and C3•G22 is disrupted, and that of T2•A23 is weak (vide supra). It is obvious from the aforementioned observations that major disruptions are induced in the stacking and the Watson−Crick hydrogen bonding three base pairs away from the lesion site in the 5′ direction. On the contrary, the hydrogen-bonding interactions between the base pairs in the 3′ direction to the lesion site A6•T19 are still present (A7•T18, C8•T17, T9•A16, T10•A15, C11•G14 base pairs), although weaker than in dsI (Figure 4); the stacking interactions are preserved in the 3′ direction to the lesion site but disrupted to an extent among G17, T18, and T19 on the basis of the absence of the imino−imino cross-peaks (Figure 5, bottom). Considering that binding takes place at base A6 at the center of the duplex and the flanking base C5 in the 5′ direction to it, there are four base pairs above C5•G20 (two C•G base pairs and two A•T base pairs) and six base pairs below A6•T19 (three C•G base pairs and three A•T base pairs), which explains the different stabilities of each stem, the severe effect of the metal binding on the shorter stem in the 5′ direction to the lesion site, and its higher exposure to the solvent (DNA breathing) (*74*, *95*).

CONCLUSION

The detailed 2D NMR data analysis performed on dsII revealed that the duplex d(CTCTC*A*ACTTCC)•d(GGAAGTTGAGAG) forms an unprecedented *intrastrand* adduct with the dirhodium unit binding residues C5 and A6 (also corroborated by enzyme digestion studies), which significantly destabilizes the duplex as indicated by the substantial decrease in its melting temperature ($\Delta T_m = -22.9$ °C) as compared to that of dsI. The reduced thermal stability of dsII is attributed to the decreased stacking of the bases and the complete disruption and/or weakening of the hydrogen bonds within the base pairs in the immediate vicinity of the modification site (C5•G20 and A6•T19) as compared to those in the parent duplex, but the effects due to the metal binding are more severe for the base pairs in the 5′ direction to the lesion site. The NMR spectroscopic data indicate that Watson−Crick hydrogen bonding is completely disrupted for the dsII lesion site C5•G20 and considerably weakened for the site A6•T19. In dsII, the bases C5 and A6 bind to *eq* positions of the dirhodium unit *cis*-$[\mathrm{Rh_2}(\mu\text{-}\mathrm{O_2CCH_3})_2(\eta^1\text{-}\mathrm{O_2CCH_3})]^+$, which retains one monodentate and two bridging acetate groups, presumably due to steric reasons. Binding of A6 takes place via N7, whereas binding of the C5 base takes place via the exocyclic N4 site, resulting in the *anti* cytosine rotamer with respect to site N3 in its metal-stabilized rare iminooxo form. Formation and stabilization of rare base forms and mispairs can be one of the factors that contribute to the antitumor activity of dirhodium compounds.

ACKNOWLEDGMENT

Professor Andy C. LiWang and Drs. Ioannis Vakonakis, Douglas A. Klewer, and Karl Koshlap are acknowledged for their help with the NMR experiments. Dr. Monique Cosman is gratefully acknowledged for helpful discussions. We also gratefully acknowledge Dr. Lisa M. Pérez for construction of the dirhodium−DNA model and helpful discussions. The Laboratory for Molecular Simulation at Texas A&M University is acknowledged for providing software and computer time. Use of the TAMU/LBMS Applications Laboratory (Laboratory of Biological Mass Spectroscopy) is also acknowledged.

SUPPORTING INFORMATION AVAILABLE

Figure S1, HPLC spectra of the reaction mixture of $\mathrm{Rh_2(O_2CCH_3)_4}$ with ssI, Figure S2, ESI-MS spectra of isolated single-stranded dirhodium adducts A−E from purification by consecutive anion exchange and reversed-phase column chromatography, Figure S3, anion exchange column chromatograms of the isolated dirhodium adducts dsA−dsE, Figure S4, thermal denaturation curves of dsI and dsII, Figure S5, CD spectra of the double-stranded DNA species dsI, dsC (green), dsD (dsII), and dsE, Figure S6, ESI-MS spectra of the enzyme digests of ssIII (single-stranded adduct D) with Phosphodiesterases I and II, Figure S7, section of the NOESY spectrum of dsI in $\mathrm{D_2O}$ at 15 °C, 280 ms mixing time, in the region of the aromatic to H1′ protons, Figure S8, aromatic to aromatic proton region from the NOESY spectrum at a 280 ms mixing time for dsI in $\mathrm{D_2O}$ at 15 °C, Figure S9, expansion of the aromatic to H3′ proton region of the NOESY spectrum for dsI in $\mathrm{D_2O}$ at 15 °C at a 280 ms mixing time, Figure S10, expansion of the aromatic to H4′ proton region of dsI from the NOESY spectrum in $\mathrm{D_2O}$ at 15 °C and a 280 ms mixing time, Figure S11, superimposed DQF-COSY spectra for dsI and dsII, Figure S12, expansion of the lr-HSQC and sr-HSQC spectra for dsI and dsII, Figure S13, expansions of NOE correlations between imino and aromatic protons for dsI and dsII from the Watergate-NOESY spectra at 15 °C, Figure S14, NOESY spectrum for dsII in $\mathrm{D_2O}$ at 15 °C and a 280 ms mixing time in the dsII proton acetate region, computational details for the molecular modeling, Figure S15, TPSS-optimized complex *cis*-$[\mathrm{Rh_2}(\mu\text{-}\mathrm{O_2CCH_3})_2(\eta^1\text{-}\mathrm{O_2CCH_3})(\mathrm{A}\text{-}N7)(\mathrm{C}\text{-}N4)(\mathrm{H_2O})]^+$, Table S1, ^{1}H NMR chemical shifts of the protons in dsI at 15 °C, and full author list for ref *46*. This material is available free of charge via the Internet at http://pubs.acs.org.

REFERENCES

1. Jamieson, E. R., and Lippard, S. J. (1999) Structure, recognition, and processing of cisplatin-DNA adducts, *Chem. Rev. 99*, 2467−2498.
2. Barnes, K. R., and Lippard, S. J. (2004) Cisplatin and related anticancer drugs: recent advances and insights, in *Metal Ions in Biological Systems* (Sigel, A., and Sigel, H., Eds.) Vol. 42, pp 143−177, Marcel Dekker, New York.
3. Jung, Y., and Lippard, S. J. (2007) Direct cellular responses to platinum-induced DNA damage, *Chem. Rev. 107*, 1388−1407.
4. Zhang, C. X., and Lippard, S. J. (2003) New metal complexes as potential therapeutics, *Curr. Opin. Chem. Biol. 7*, 481−489.
5. van Zutphen, S., and Reedijk, J. (2005) Targeting platinum antitumour drugs: overview of strategies employed to reduce systemic toxicity, *Coord. Chem. Rev. 249*, 2845−2853.
6. Clarke, M. J., Zhu, F., and Frasca, D. R. (1999) Non-platinum chemotherapeutic metallopharmaceuticals, *Chem. Rev. 99*, 2511−2533.
7. Kohno, K. (2005) Cisplatin resistance and transcription factors, *Curr. Med. Chem.: Anti-Cancer Agents 5*, 15−27.
8. Chifotides, H. T., and Dunbar, K. R. (2005) Rhodium compounds, in *Multiple Bonds Between Metal Atoms* (Cotton, F. A., Murillo, C., and Walton, R. A., Eds.) 3rd ed., Chapter 12, pp 465−589, Springer-Science and Business Media, Inc., New York.
9. Hughes, R. G., Bear, J. L., and Kimball, A. P. (1972) Synergistic effect of rhodium acetate and arabinosylcytosine on L1210, *Proc. Am. Assoc. Cancer Res. 13*, 120.
10. Howard, R. A., Kimball, A. P., and Bear, J. L. (1979) Mechanism of action of tetra-μ-carboxylatodirhodium(II) in L1210 tumor suspension culture, *Cancer Res. 39*, 2568−2573.
11. Erck, A., Rainen, L., Whileyman, J., Chang, I. M., Kimball, A. P., and Bear, J. (1974) Studies of rhodium(II) carboxylates as potential antitumor agents, *Proc. Soc. Exp. Biol. Med. 145*, 1278−1283.
12. Bear, J. L., Gray, H. B., Jr., Rainen, L., Chang, I. M., Howard, R., Serio, G., and Kimball, A. P. (1975) Interaction of rhodium(II) carboxylates with molecules of biologic importance, *Cancer Chemother. Rep. I 59*, 611−620.
13. Zyngier, S., Kimura, and Najjar, E. R. (1989) Antitumor effects of rhodium(II) citrate in mice bearing Ehrlich tumors, *Braz. J. Med. Biol. Res. 22*, 397−401.
14. Bear, J. L. (1986) in *Precious Metals 1985: Proceedings of the Ninth International Precious Metals Conference* (Zysk, E. D., and Bonucci, J. A., Eds.) pp 337−344, International Precious Metals, Allentown, PA.
15. Chifotides, H. T., and Dunbar, K. R. (2005) Interactions of metal-metal-bonded antitumor active complexes with DNA fragments and DNA, *Acc. Chem. Res. 38*, 146−156.
16. Sorasaenee, K., Fu, P. K.-L., Angeles-Boza, A. M., Dunbar, K. R., and Turro, C. (2003) Inhibition of transcription *in vitro* by anticancer active dirhodium(II) complexes, *Inorg. Chem. 42*, 1267−1271.
17. Chifotides, H. T., Fu, P. K.-L., Dunbar, K. R., and Turro, C. (2004) Effect of equatorial ligands of dirhodium(II,II) complexes on the efficiency and mechanism of transcription inhibition *in vitro*, *Inorg. Chem. 43*, 1175−1183.
18. Howard, R. A., Spring, T. G., and Bear, J. L. (1976) The interaction of rhodium(II) carboxylates with enzymes, *Cancer Res. 36*, 4402−4405.
19. Pneumatikakis, G. and Hadjiliadis, N. (1979) Interactions of tetrakis-μ-acetatodirhodium(II) with adenine nucleosides and nucleotides, *J. Chem. Soc., Dalton Trans.* 596−599.
20. Farrell, N. (1981) Adenine and adenosine derivatives of rhodium acetate, *J. Inorg. Biochem. 14*, 261−265.
21. Rubin, J. R., Haromy, T. P., and Sundaralingam, M. (1991) Structure of the anti-cancer drug complex tetrakis(μ-acetato)bis-(1-methyladenosine)dirhodium(II) monohydrate, *Acta Crystallogr. C47*, 1712−1714.
22. Aoki, K., and Salam, M. (2002) Interligand interactions affecting specific metal bonding to nucleic acid bases. A case of $[\mathrm{Rh_2(OAc)_4}]$, $[\mathrm{Rh_2(HNOCCF_3)_4}]$, and $[\mathrm{Rh_2(OAc)_2(HNOCCF_3)_2}]$ toward purine nucleobases and nucleosides, *Inorg. Chim. Acta 339*, 427−437.
23. Catalan, K. V., Mindiola, D. J., Ward, D. L., and Dunbar, K. R. (1997) A novel dirhodium compound with neutral, bridging 9-ethyladenine ligands, *Inorg. Chem. 36*, 2458−2460.
24. Catalan, K. V., Hess, J. S., Maloney, M. M., Mindiola, D. J., Ward, D. L., and Dunbar, K. R. (1999) Reactions of DNA purines with

dirhodium formamidinate compounds that display antitumor behavior, *Inorg. Chem. 38*, 3904−3913.

25. Chifotides, H. T., and Dunbar, K. R. (2007) Unprecedented head-to-head right handed cross-links between the antitumor bis(*μ-N,N′*-di-*p*-tolylformamidinate) dirhodium(II,II) core and the dinucleotide d(ApA) with the adenine bases in the rare imino form, *J. Am. Chem. Soc. 129*, 12480−12490.
26. Aoki, K., and Salam, Md. A. (2001) Interligand interactions affecting specific metal bonding to nucleic acid bases: the tetrakis-(m-trifluoroacetamidato)dirhodium(II)-cytosine system. Crystal structures of $[Rh_2(CF_3CONH)_4(\text{cytosine})]$ and $[Rh_2(CF_3CONH)_4(\text{cytosine})]\cdot H_2O$, *Inorg. Chim. Acta 316*, 50−58.
27. Dunbar, K. R., Matonic, J. H., Saharan, V. P., Crawford, C. A., and Christou, G. (1994) Structural Evidence for a new metal-binding mode for guanine bases- implications for the binding of dinuclear antitumor agents to DNA, *J. Am. Chem. Soc. 116*, 2201−2202.
28. Crawford, C. A., Day, E. F., Saharan, V. P., Folting, K., Huffman, J. C., Dunbar, K. R., and Christou, G. (1996) *N7,O6* bridging 9-ethylguanine (9-EtGH) groups in dinuclear metal-netal bonded complexes with bond orders of one, two or four, *Chem. Commun.* 1113−1114.
29. Deubel, D. V., and Chifotides, H. T. (2007) Guanine binding to dirhodium tetracarboxylate anticancer complexes: quantum chemical calculations unravel an elusive mechanism, *Chem. Commun.* 3438−3440.
30. Chifotides, H. T., Koshlap, K. M., Pérez, L. M., and Dunbar, K. R. (2003) Unprecedented head-to-head conformers of d(GpG) bound to the antitumor active compound tetrakis (*μ*-carboxylato)-dirhodium(II,II), *J. Am. Chem. Soc. 125*, 10703−10713.
31. Chifotides, H. T., Koshlap, K. M., Pérez, L. M., and Dunbar, K. R. (2003) Novel binding interactions of the DNA fragment d(pGpG) cross-linked by the antitumor active compound tetrakis-(*μ*-carboxylato)dirhodium(II,II), *J. Am. Chem. Soc. 125*, 10714−10724.
32. Chifotides, H. T., and Dunbar, K. R. (2006) Head-to-head cross-linked adduct between the antitumor unit bis(*μ-N,N′*-di-*p*-tolyl-formamidinate) dirhodium(II,II) and the DNA fragment d(GpG), *Chem.*−*Eur. J. 12*, 6458−6468.
33. Dunham, S. U., Chifotides, H. T., Mikulski, S., Burr, A. E., and Dunbar, K. R. (2005) Covalent binding and interstrand cross-linking of duplex DNA by dirhodium(II,II) carboxylate compounds, *Biochemistry 44*, 996−1003.
34. Angeles-Boza, A. M., Chifotides, H. T., Aguirre, J. D., Chouai, A., Fu, P. K.-L., Dunbar, K. R., and Turro, C. (2006) Dirhodium-(II,II) complexes: Molecular characteristics that affect in vitro activity, *J. Med. Chem. 49*, 6841−6847.
35. Asara, J. M., Hess, J. S., Lozada, E., Dunbar, K. R., and Allison, J. (2000) Evidence for binding of dirhodium bis-acetate units to adjacent GG and AA sites on single-stranded DNA, *J. Am. Chem. Soc. 122*, 8−13.
36. Chifotides, H. T., Koomen, J. M., Kang, M. J., Tichy, S. E., Dunbar, K. R., and Russell, D. H. (2004) Binding of DNA purine sites to dirhodium compounds probed by mass spectrometry, *Inorg. Chem. 43*, 6177−6187.
37. Kang, M., Chouai, A., Chifotides, H. T., and Dunbar, K. R. (2006) 2D NMR spectroscopic evidence for unprecedented interactions of *cis*-$[Rh_2(\text{dap})(\mu\text{-}O_2CCH_3)_2(\eta^1\text{-}O_2CCH_3)(CH_3OH)](O_2CCH_3)$ with a DNA oligonucleotide: Combination of intercalative and coordinative binding, *Angew. Chem., Int. Ed. 45*, 6148−6151.
38. Markley, J. L., Bax, A., Arata, Y., Hilbers, C. W., Kaptein, R., Sykes, B. D., Wright, P. E., and Wuthrich, K. (1998) IUPAC-IUBMB-IUPAB Inter-union task group on the standardization of data bases of protein and nucleic acid structures determined by NMR spectroscopy, *Pure Appl. Chem. 70*, 117−142.
39. Piotto, M., Saudek, V., and Sklenar, V. (1992) Gradient-tailored excitation for single-quantum NMR spectroscopy of aqueous solutions, *J. Biomol. NMR 2*, 661−665.
40. Bax, A., Farley, K. A., and Walker, G. S. (1996) Increased HMBC sensitivity for correlating poorly resolved proton multiplets to ^{13}C using selective or semi-selective pulses, *J. Magn. Reson., Ser. A 119*, 134−138.
41. Delaglio, F., Grzesiek, S., Vuister, G. W., Zhu, G., Pfeifer, J., and Bax, A. (1995) NMRPipe: a multidimensional spectral processing system based on UNIX pipes, *J. Biomol. NMR 6*, 277−293.
42. Case, D. A., Cheatham, T. E., III, Darden, T., Gohlke, H., Luo, R., Merz, K. M., Jr., Onufriev, A., Simmerling, C., Wang, B., and Woods, R. (2005) The Amber biomolecular simulation programs, *J. Comput. Chem. 26*, 1668−1688.
43. Cotton, F. A., DeBoer, B. G., LaPrade, M. D., Pipal, J. R., and Ucko, D. A. (1971) The crystal and molecular structures of dichromium tetraacetate dihydrate and dirhodium tetraacetate dihydrate, *Acta Crystallogr. B27*, 1664.
44. Tao, J. M., Perdew, J. P., Staroverov, V. N., and Scuseria, G. E. (2003) Climbing the density functional ladder: Nonempirical meta-generalized gradient approximation designed for molecules and solids, *Phys. Rev. Lett. 91*, 146401.
45. Dunlap, B. I. (2000) Robust and variational fitting: Removing the four-center integrals from center stage in quantum chemistry, *J. Mol. Struct.*: *THEOCHEM 529*, 37.
46. Gaussian 03, Revision D.02 (2004) Gaussian, Inc., Wallingford, CT (full reference in Supporting Information).
47. (a) Hehre, W. J., Ditchfield, R., and Popl, J. A. (1972) Self-consistent molecular orbital methods. XII. Further extensions of Gaussian-type basis sets for use in molecular orbital studies of organic molecules, *J. Chem. Phys. 56*, 2257. (b) Krishnan, R., Binkley, J. S., Seeger, R., and Pople, J. A. (1980) Self-consistent molecular orbital methods. XX. A basis set for correlated wave functions, *J. Chem. Phys. 72*, 650.
48. Godbout, N., Salahub, D. R., Andzelm, J., and Wimmer, E. (1992) Optimization of Gaussian-type basis sets for local spin density functional calculations. Part I. Boron through neon, optimization technique and validation, *Can. J. Chem. 70*, 560.
49. Poklar, N., Pilch, D. S., Lippard, S. J., Redding, E. A., Dunham, S. U., and Breslauer, K. J. (1996) Influence of cisplatin intrastrand crosslinking on the conformation, thermal stability, and energetics of a 20-mer DNA duplex, *Proc. Natl. Acad. Sci. U.S.A. 93*, 7606−7611.
50. Cohen, G. L., Ledner, J. A., Bauer, W. R., Ushay, H. M., Caravana, C., and Lippard, S. J. (1980) Sequence dependent binding of *cis*-dichlorodiammineplatinum(II) to DNA, *J. Am. Chem. Soc. 102*, 2487−2488.
51. Tullius, T. D., and Lippard, S. J. (1981) *Cis*-Diamminedichloro-platinum(II) binds in a unique manner to oligo(dG).oligo(dC) sequences in DNA-a new assay using exonuclease III, *J. Am. Chem. Soc. 103*, 4620−4622.
52. Inagaki, K., Kasuya, K., and Kidani, Y. (1984) Determination of platinum binding bases in oligonucleotides. Application of exonuclease digestion method, *Inorg. Chim. Acta 91*, L13−L15.
53. Wuthrich, K. (1986) *NMR of Proteins and Nucleic Acids*, John Wiley & Sons, Inc., New York.
54. The stability of dsII at room temperature is supported by the fact that, in the DQF-COSY spectrum of the adduct, the H5/H6 cross-peaks of the cytosine residues remain at the same positions after the sample has been left at room temperature for several weeks (Figure S11).
55. Pneumatikakis G., and Hadjiliadis, N. (1979) Interactions of tetrakis-*μ*-acetato-dirhodium(II) with adenine nucleosides and nucleotides, *J. Chem. Soc., Dalton Trans.* 596−599.
56. Yang, D., van Boom, S. G. E., Reedijk, J., van Boom, J. H., and Wang, A. H.-J. (1995) Structure and isomerization of an intrastrand cisplatin-cross-linked octamer DNA, *Biochemistry 34*, 12912−12920.
57. Gelasco, A., and Lippard, S. J. (1998) NMR solution structure of a DNA dodecamer duplex containing a *cis*-diammineplatinum-(II) d(GpG) intrastrand cross-link, the major adduct of the anticancer drug cisplatin, *Biochemistry 37*, 9230−9239.
58. Qu, Y., Scarsdale, N. J., Tran, M.-C., and Farrell, N. (2003) Cooperative effects in long range 1,4 DNA-DNA interstrand cross-links formed by polynuclear platinum complexes: an unexpected *syn* orientation of adenine bases outside the binding sites, *J. Biol. Inorg. Chem. 8*, 19−28.
59. Liu, Y., Pacifico, C., Natile, G., and Sletten, E. (2001) Antitumor *trans* platinum complexes can form cross-links with adjacent purine groups, *Angew. Chem., Int. Ed. 40*, 1226−1228.
60. Sowers, L. C., Fazakerley, G. V., Kim, H., Dalton, L., and Goodman, M. F. (1986) Variation of nonexchangeable proton resonance chemical shifts as a probe of aberrant base pair formation in DNA, *Biochemistry 25*, 3983−3988.
61. Schöllhorn, H., Beyerle-Pfnür, R., Thewalt, U., and Lippert, B. (1986) Unusual four-membered chelate rings of Pt^{IV} with a cytosine nucleobase, *J. Am. Chem. Soc. 108*, 3680−3688.
62. Müller, J., Glahé, F., Freisinger, E., and Lippert, B. (1999) A major, pH-induced stereochemical switch of pairs of *trans*-oriented ligands in complexes of *trans*-a_2Pt^{II} ($a = NH_3$, CH_3NH_2), *Inorg. Chem. 38*, 3160−3166.

63. Müller, J., Zangrando, E., Pahlke, N., Freisinger, E., Randaccio, L., and Lippert, B. (1998) Affinity of the iminooxo tautomer anion of 1-methylcytosine in *trans*-$[\mathrm{Pt(NH_3)_2(1\text{-}MeC\text{-}N_4)_2}]^{2+}$ for heterometals, *Chem.—Eur. J. 4*, 397−405.
64. Roitzsch, M., Garijo, Añorbe, M., Sanz, Miguel, P. J., Müller, B., and Lippert, B. (2005) The role of intramolecular hydrogen bonding on nucleobase acidification following metal coordination: possible implications of an "indirect" role of metals in acid−base catalysis of nucleic acids, *J. Biol. Inorg. Chem. 10*, 800−812.
65. Sanz, Miguel, P. J., Lax, P., and Lippert, B. (2006) $\mathrm{(Dien)M^{II}}$ (M = Pd, Pt) and $\mathrm{(NH_3)_3Pt^{II}}$ complexes of 1-methylcytosine: Linkage and rotational isomerism, metal-promoted deamination, and pathways to dinuclear species, *J. Inorg. Biochem. 100*, 980−991.
66. Shen, W.-Z., Gupta, D., and Lippert, B. (2005) Cyclic trimer versus *head-tail* dimer in metal-nucleobase complexes: importance of relative orientation (*syn*, *anti*) of the metal entities and relevance as a metallaazacrown compound, *Inorg. Chem. 44*, 8249−8258.
67. The orientation of the metal at N4 relative to the N3 site of cytosine may be *syn* or *anti*, and the cytosine is in the rare iminooxo form. In the case of *anti* orientation, the metal is on the side of the C5 site.
68. Lippert, B. (2005) Alterations of nucleobase $\mathrm{pK_a}$ values upon metal coordination: origins and consequences, in *Progress in Inorganic Chemistry* (Karlin, K. D., Ed.) Vol. 54, pp 385−447, John Wiley & Sons, Inc., New York.
69. Teuben, J.-M., Bauer, C., Wang, A. H.-J., and Reedijk, J. (1999) Solution structure of a DNA duplex containing a *cis*-diammine-platinum(II) 1,3-d(GTG) intrastrand cross-link, a major adduct in cells treated with the anticancer drug carboplatin, *Biochemistry 38*, 12305−12312.
70. Huang, H., Zhu, L., Reid, B. R., Drobny, G. P., and Hopkins, P. B. (1995) Solution structure of a cisplatin-induced DNA interstrand cross-link, *Science 270*, 1842−1845.
71. Stoldt, M., Porzel, A., Adam, G., and Brandt, W. (1997) Side chain conformation of the growth-promoting phytormones brassinolide and 24-epibrassinolide, *Magn. Reson. Chem. 35*, 629−636.
72. Seeliger, M. A., Spichty, M., Kelly, S. E., Bycroft, M., Freund, S. M. V., Karplus, M., and Itzhaki, L. S. (2005) Role of conformational heterogeneity in domain swapping and adapter function of the Cks proteins, *J. Biol. Chem. 280*, 30448−30459.
73. Volk, D. E., Rice, J. S., Luxon, B. A., Yeh, H. J. C., Liang, C., Xie, G., Sayer, J. M., Jerina, D. M., and Gorenstein, D. G. (2000) NMR evidence for *syn-anti* interconversion of a trans opened (10*R*)-dA adduct of benzo[*a*]pyrene (7*S*,8*R*)-diol (9*R*,10*S*)-epoxide in a DNA duplex, *Biochemistry 39*, 14040−14053.
74. Cho, B. B., Beland, F. A., and Marques, M. M. (1992) NMR structural studies of a 15-mer DNA sequence from a ras proto-oncogene, modified at the first base of codon 61 with the carcinogen 4-aminobiphenyl, *Biochemistry 31*, 9587−9602.
75. Janik, M. B. L., Hegmans, A., Freisinger, E., and Lippert, B. (1999) Reactivity of an extremely sterically crowded monofunctional Pt complex, $[\mathrm{Pt(1\text{-}MeC\text{-}}\mathit{N3})_3\mathrm{(H_2O)}]^{2+}$ (1-MeC = 1-methylcytosine), toward model nucleobases and selectivity toward guanine in single- and double-stranded deoxyoligonucleotides, *J. Biol. Inorg. Chem. 4*, 130−139.
76. Mancin, F., and Chin, J. (2002) An artificial guanine that binds cytidine through the cooperative interaction of metal coordination and hydrogen bonding, *J. Am. Chem. Soc. 124*, 10946−10947.
77. Teletchéa, S., Komeda, S., Teuben, J.-M., Elionzo-Riojas, M.-A., Reedijk, J., and Kozelka, J. (2006) A pyrazolato-bridged dinuclear platinum(II) complex induces only minor distortions upon DNA-binding, *Chem.—Eur. J. 12*, 3741−3753.
78. Brown, K., Hingerty, B. E., Guenther, E. A., Krishnan, V. V., Broyde, S., Turteltaub, K. W., and Cosman, M. (2001) Solution structure of the 2-amino-1-methyl-6-phenylimidazo[4,5-*b*]pyridine C8-deoxyguanosine adduct in duplex DNA, *Proc. Natl. Acad. Sci. U.S.A. 98*, 8507−8512.
79. Somerville, L., Krynetski, E. Y., Krynetskaia, N. F., Beger, R. D., Zhang, W., Marhefka, C. A., Evans, W. E., and Kriwacki, R. W. (2003) Structure and dynamics of thioguanine-modified duplex DNA, *J. Biol. Chem. 278*, 1005−1011.
80. Dhavan, G. M., Lapham, J., Yang, S., and Crothers, D. M. (1999) Decreased imino proton exchange and base-pair opening in the IHF-DNA complex measured by NMR, *J. Mol. Biol. 288*, 659−671.
81. In the imino proton region (11.0−14.5 ppm) of the 1D NMR spectrum of dsII in 90% $\mathrm{H_2O}$/10% $\mathrm{D_2O}$ at 2 °C, the imino GN1 and TN3 protons of all the bases that are hydrogen-bonded in the metalated duplex give rise to sharp resonances, except for that of G20N1, which gives a very broad upfield resonance at this temperature because it is not hydrogen-bonded to C5N3.
82. Heerschap, A., Haasnoot, C. A. G., and Hilbers, C. W. (1983) Nuclear magnetic resonance studies on yeast $\mathrm{tRNA^{Phe}}$. III. Assignments of the iminoproton resonances of the tertiary structure by means of nuclear Overhauser effect experiments at 500 MHz, *Nucleic Acids Res. 11* (13), 4501−4520.
83. Crawford, C. A., Matonic, J. H., Streib, W. E., Huffman, J. C., Dunbar, K. R., and Christou, G. (1993) Reaction of 2,2′-bipyridine (bpy) with dirhodium carboxylates: Mono-bpy products with variable chelate binding modes and insights into the reaction mechanism, *Inorg. Chem. 32*, 3125−3133.
84. Yoshimura, T., Umakoshi, K., and Sasaki, Y. (2003) Structural studies on the stepwise chelating processes of bidentate 2-(aminomethyl)pyridine and tridentate bis(2-pyridylmethyl)amine toward an acetate-bridged dirhodium(II) center, *Inorg. Chem. 42*, 7106−7115.
85. Kozelka, J., Fouchet, M.-H., and Chottard, J.-C. (1992) H8 chemical shifts in oligonucleotides cross-linked at a GpG sequence by cis-$\mathrm{Pt(NH_3)_2}^{2+}$: a clue to the adduct structure, *Eur. J. Biochem. 205*, 895−906.
86. Hesselmann, A., Jansen, G., and Schütz, M. (2006) Interaction energy contributions of H-bonded and stacked structures of the AT and GC DNA base pairs from the combined density functional theory and intermolecular perturbation theory approach, *J. Am. Chem. Soc. 128*, 11730−11731.
87. Delcourt, S. G., and Blake, R. D. (1991) Stacking energies in DNA, *J. Biol. Chem. 266*, 15160−15169.
88. Sherman, S. E., and Lippard, S. J. (1987) Structural aspects of platinum anticancer drug interactions with DNA, *Chem. Rev. 87*, 1153−1181.
89. Chifotides, H. T., Dunbar, K. R., Katsaros, N., and Pneumatikakis, G. (1994) Synthesis, spectroscopic and magnetic resonance studies of mercury(II) and methylmercury(II) complexes of azathioprine, a biologically active mercaptopurine derivative, *J. Inorg. Biochem. 55*, 203−216.
90. Rubin, J. R., and Sundaralingam, M. J. (1984) Crosslinking of tRNA by the carcinostatic agent dirhodium tetraacetate, *J. Biomol. Struct. Dyn. 2*, 525−530.
91. Lippert, B. (2000) Multiplicity of metal ion binding patterns to nucleobases, *Coord. Chem. Rev. 200-202*, 487−516.
92. Van de Ven, F. J. M., and Hilbers, C. W. (1988) Nucleic acids and nuclear magnetic resonance, *Eur. J. Biochem. 178*, 1−38.
93. Sponer, J., Sponer, J. E., Gorb, L., Leszczynski, J., and Lippert, B. (1999) Metal-stabilized rare tautomers and mispairs of DNA bases: N6-metalated adenine and N4-metalated cytosine, theoretical and experimental views, *J. Phys. Chem. A 103*, 11406−11413.
94. Quigley, G. J., Ughetto, G., van der Marel, G. A., van Boom, J. H., Wang, A. H.-J., and Rich, A. (1986) Non-Watson-Crick G•C and A•T base pairs in a DNA-antibiotic complex, *Science 232*, 1255−1258.
95. Marzilli, L., Saad, J. S., Kuklenyik, Z., Keating, K. A., and Xu, Y. (2001) Relationship of solution and protein-bound structures of DNA duplexes with the major intrastrand cross-link lesions formed on cisplatin binding to DNA, *J. Am. Chem. Soc. 123*, 2764−2770.
96. Parkinson, J. A., Chen, Y., del Socorro Murdoch, P., Guo, Berners-Price, Z., S. J., Brown, T., and Sadler, P. (2000) Sequence-dependent bending of DNA induced by cisplatin: NMR structures of an A•T rich 14-mer duplex, *Chem.—Eur. J. 6*, 3636−3644.
97. Dornberger, U., Leijon, M., and Fritzsche, H. (1999) High base pair opening rates in tracts of GC base pairs, *J. Biol. Chem. 274*, 6957−6962.
98. Kochoyan, M., Leroy, J. L., and Guéron, M. (1987) Proton exchange and base pair lifetimes in a deoxy-duplex containing a purine-pyrimidine step in the duplex of inverse sequence, *J. Mol. Biol. 196*, 599−609.
99. Herman, F., Kozelka, J., Stoven, V., Guittet, E., Girault, J.-P., Huynh-Dinh, T., Igolen, J., Lallemand, J.-Y., and Chottard, J.-C. (1990) A d(GpG)-platinated decanucleotide duplex is kinked; an extended NMR and molecular mechanics study, *Eur. J. Biochem. 194*, 119−133.
100. Elizondo-Riojas, M.-A., and Kozelka, J. (2001) Unrestrained 5 ns molecular dynamics simulation of a cisplatin-DNA 1,2-GG adduct provides a rationale for the NMR features and reveals increased conformational flexibility at the platinum binding site, *J. Mol. Biol. 314*, 1227−1243.

BI701901C